Tuning needle-like precipitation for enhanced strength-ductility synergy in a non-equiatomic FeNiCoCuTi high-entropy alloy

Liran Huang^{1,2}, Zhiming Li³, Weiping Chen^{1,2}, and ^{*}Zhiqiang Fu^{1,2}

Guangdong Key Laboratory for Advanced Metallic Materials Processing, South China University of Technology, Guangzhou,
 Guangdong 510641, China;
 National Engineering Research Center of Near-net-shape Forming for Metallic Materials, South China
 University of Technology, Guangzhou 510641, China;
 School of Materials Science and Engineering, Central South University,
 Changsha 410083, China

*Corresponding address: e-mail: zhiqiangfu2019@scut.edu.cn

Abstract: Precipitation strengthening is an effective strengthening method widely utilized in high-entropy alloys (HEAs) with a single-phased face-centered cubic (fcc) structure. Among the various reinforcing phases, the coherent L12 phase is the most commonly employed, with additional instances including the body-centered cubic (bcc), the B2 phase and σ phase. The η -D024 phase, which shares an ordered Ni3Ti-type structure as the L12 phase; however, the strengthening effect of the sole η -D024 phase in fcc-structured alloys remains to be further explored. In this study, microstructure evolution, phase transformation, and mechanical behaviors of a novel Fe27Ni27Co26Cu10Ti10 HEA were systematically investigated. After high-temperature heat treatment, the microstructure of the studied HEA transformed from a combination of the fcc, L12, Cu-rich, and η phases in the as-cast state to the fcc+ η structure in the heat-treated state. Meanwhile, the mechanical properties of the heat-treated HEA were dramatically improved, with total elongation increasing from \sim 0.9% to \sim 7.5% and ultimate tensile strength of \sim 925 MPa. The enhanced ductility of the alloy can be attributed to the strong hindering effect of numerous needle-like η phase at the grain boundaries, which restricted crack propagation and dislocation movement. This study develops a novel η -strengthened non-equiatomic FeNiCoCuTi HEA, expanding the selection of available reinforcing phases in fcc-structured alloys and providing valuable insights into the phase transition and strengthening effect of the η -D024 phase.

Keywords: High-entropy alloys; η -D024 phase; Microstructure; Phase transformation; Mechanical properties

1 Introduction

High-entropy alloys (HEAs) or multi-principal-element alloys (MPEAs) with various excellent properties and unique characteristics have become one of the hot research topics in metal materials [1, 2]. Faced-centered cubic (fcc) structured HEAs are particularly notable for their high ductility, outstanding impact toughness, attractive strain hardening capacity, and good corrosion resistance [3-5]. However, due to the inherent feature of the crystal structure, the yield strength of fcc-structured HEAs, especially polycrystalline HEAs, is usually unsatisfactory, making it challenging to meet industrial demands [6, 7]. Plentiful studies have focused on improving the moderate strength of the fcc-structured HEAs, with commonly used strengthening strategies including solid solution strengthening, grain refinement strengthening, precipitation strengthening, strengthening[8-11]. heterogeneous Precipitation

strengthening stands out among multiple strengthening mechanisms by its remark-able strengthening effect and adjustable performance, achievable through simplified alloying and heat treatment processes [12, 13].

Numerous reinforcing phases can be introduced into single-phase fcc matrix, including ordered fcc-structured L1₂, disordered body-centered cubic (bcc), ordered bcc-structured B2, topological closed packed (tcp) structured σ , μ and Laves, ordered hexagonal close-packed (hcp) structured η -D0₂₄ and so on [14–18]. The ordered L1₂ phase is the most widely used strengthening phase in fcc-structured HEAs, which is completely coherent with the disordered fcc phase. Therefore, introducing the L1₂ phase can significantly improve strength without a substantial loss in ductility [19, 20]. For instance, Yang et al [14]. reported a L1₂-strengthened Ni-30Co-13Fe-15Cr-6Al-6Ti-0.1B HEA by duplex-aging treatment, achieving a remarkable

improvement of strength and ductility. Conversely, the ordered η -D0₂₄ phase, which shares the same Ni₃Ti-type structure as the L1₂ phase, is generally considered deleterious in fcc-structured alloys^[21]. In fact, the η -D0₂₄ phase with proper distribution and volume fraction can also enhance strength under the premise of limited ductility reduction^[22]. Since the η -D0₂₄ phase typically occurs in conjunction with other precipitates, the strengthening mechanisms of the η -D0₂₄ phase alone are rarely studied^[23].

It is quite challenging to introduce the sole η-D0₂₄ phase in the fcc-structured HEAs without forming other precipitates. Based on our previous research, we can know that the L1₂ phase and η-D0₂₄ phase can transform into one another under specific conditions^[24]. Therefore, the objective of this work is to achieve a microstructure comprising fcc and n phases via the combination of tailoring composition and simplified heat treatment. Ti is the crucial element to promote the formation of the η-D0₂₄ phase^[25], so a high concentration of Ti (10 at.%) was involved in the alloy. In the present work, we proposed a non-equiatomic Fe₂₇Ni₂₇Co₂₆Cu₁₀Ti₁₀ (at.%) HEA. The designed HEA was arc melted to obtain the as-cast sample, which was subsequently held at 1000°C for 4 h to obtain the heat-treated sample. The microstructure evolution and phase transformation during the heat treatment progress were discussed in detail, and the impact of the sole η-D0₂₄ phase on the mechanical properties of the FeNiCo fcc-structured HEA was investigated systematically.

2 Experimental procedures

2.1 Materials preparation

The investigated alloy with a nominal composition of Fe₂₇Ni₂₇Co₂₆Cu₁₀Ti₁₀ (at.%) was fabricated *via* magnetic levitation melting. Pure bulk metals of Fe, Ni, Co, Cu, and Ti with high purity (≥99.5 wt.%) were used as raw materials. The ingots were remelted at least five times to avoid element segregation, and the entire melting process was performed under a high purity argon atmosphere. The as-cast samples were homogenized at 1000°C for 4 h with flowing argon gas to assuage elemental segregation during solidification and followed by water quenching, then the heat-treated samples were obtained.

2.2 Microstructure characterization

The phase constitution of the as-cast and heat-treated samples was identified by X-ray diffractometer (XRD, X'Pert Pro PANalytical) using Cu-K α radiation with a scanning range of 20°-100°. The electron backscattered diffraction (EBSD, JEOL 7100F equipped with a field

emission gun) equipped with a field emission gun) measurement with an accelerating voltage of 15 kV was conducted to observe the average grain size and grain orientation. The microstructure of the studied HEA was characterized using scanning electron microscopy (SEM, FE-SEM, JEOL, JSM-7800F) equipped with a backscattering electron (BSE) detector. Further fine microstructure. crystal structure. and chemical composition were analyzed high-resolution by transmission electron microscopy (TEM, FEI Talos F200X) equipped with selected area electron diffraction (SAED) and energy dispersive spectroscopy (EDS) detector. EDS measurement was conducted on the scanning transmission electron microscopy (STEM) mode. To accurately investigate the chemical distribution at the sub-nanometer scale, atom probe tomography (APT, LEAPTM 3000X HR) was employed with the acquisition temperature of 70 K, the pulse frequency of 200 kHz and pulse fraction of 15%. The target detection rate was set to be 0.4%, which is an average of 4 detection events per 1000 pulses. The 3-dimensional (3D) atomic map reconstruction, visualization and all data analysis were performed using the IVAS® 3.6.14 software. The needle-shaped APT specimen was fabricated by dual beam focused-ion-beam (FIB, Helios Nanolab600/600i).

2.3 Mechanical testing

The mechanical properties of the as-cast and heat-treated samples were investigated by tensile testing at room temperature. The dog-bone shaped tensile specimens with a gauge dimension of 10 mm×2.5 mm×1.0 mm (length×width×thickness) were fabricated by electrical discharge machining. The tensile tests were carried out on a Zwick/Roell Z020 universal testing machine with an engineering rate of 1×10⁻³ s⁻¹ at room temperature, and each sample was repeated at least three times to ensure the reliability of the data. After tensile testing, the fracture morphology of the tensile specimens was characterized by SEM on the secondary electron mode.

3 Results and discussion

3.1 Microstructure evolution

As shown in Fig. 1, both XRD patterns of the as-cast and heat-treated Fe₂₇Ni₂₇Co₂₆Cu₁₀Ti₁₀ HEA exhibit two types of diffraction peaks, corresponding to the fcc structure and η structure, respectively. The peaks representing the fcc structure have more numbers and higher peak intensities than those peaks representing the η structure, indicating that the fcc may be the primary phase in the as-cast and heat-treated sample. The EBSD phase map

and inverse pole figure (IPF) map in Fig. 2 reveal that as-cast Fe₂₇Ni₂₇Co₂₆Cu₁₀Ti₁₀ HEA is equiaxed grains with a single-phase fcc structure. The presence of only the fcc phase in the phase map (Fig. 2(a)) may be due to too small size or too low volume fraction of the η phase. Additionally, grain boundaries of the as-cast sample are predominantly composed of high-angle grain boundaries (HAGBs, higher than 15°) with a minor presence of low-angle grain boundaries (LAGBs, 2°-15°). The average grain size of the as-cast sample is obtained to be ~37.3 μ m.

The microstructure of the as-cast Fe₂₇Ni₂₇Co₂₆Cu₁₀Ti₁₀ HEA is presented in Fig. 3. In the low- and high-magnification SEM images (Figs. 3(a-b)), the equiaxed grains (grey region) and some uncertain phases (white region) near the grain boundaries can be visibly observed. When the region near the grain boundaries is magnified, a large amount of near-spherical precipitates can be observed, as shown in Figs. 3(b-c). Other magnified images of the grain boundary (Figs. 3(d-e)) display some needle-like phase generated at the grain boundaries. The crystal structure of these two phases will be identified by TEM and APT analysis in the later section. In contrast, the high-magnification SEM image of the transgranular region (Fig. 3(f)) manifests the absence of precipitates in the grain interior. Additionally, the EDS results of the point 1, point 2, and point 3 are summarized in Table 1. Point 1, which represents the grain interior of the as-cast sample, is ~30.80 at.%(Fe), ~26.16 at.%(Ni), ~26.42 at.%(Co), ~8.87 at.%(Cu), and ~7.75 at.%(Ti), indicating a chemical composition close to the nominal component. Meanwhile, the EDS results of points 2 and 3 demonstrate a preferential concentration of Ni-Ti in the needle-like phase and a slight enrichment tendency of Ni-Cu-Ti in the near-spherical precipitates, respectively.

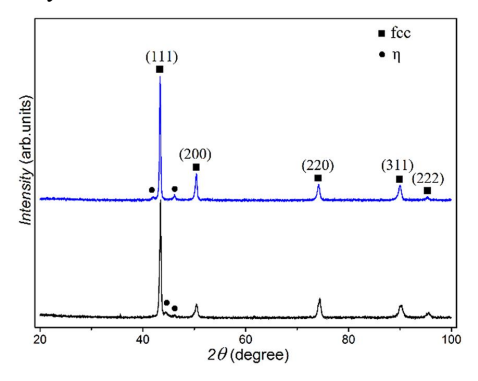


Fig. 1: XRD patterns of the as-cast (black line) and heat-treated (blue line) Fe27Ni27Co26Cu10Ti10 HEA samples.

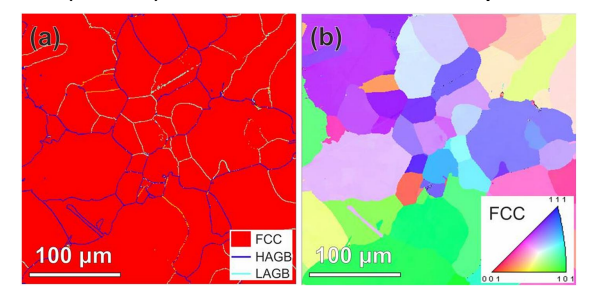


Fig. 2: EBSD phase map (a) and inverse pole figure map (b) of the as-cast Fe27Ni27Co26Cu10Ti10 HEA. HAGB and LAGB in (a) refer to high and low angle grain boundaries, respectively.

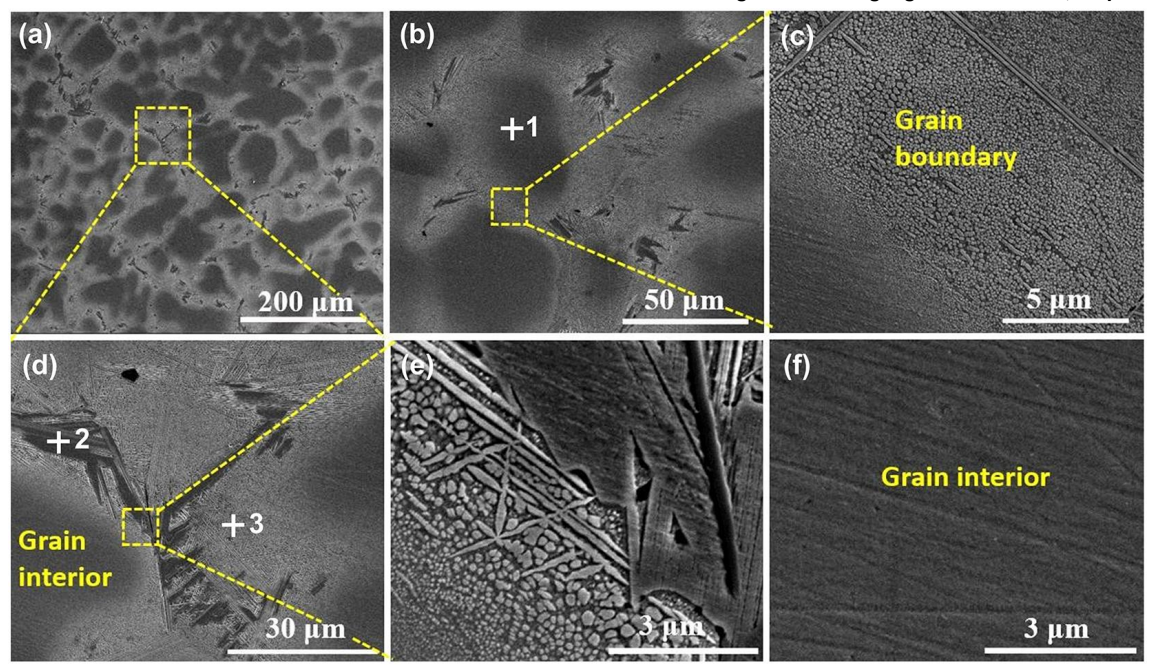


Fig. 3: SEM images of the as-cast Fe27Ni27Co26Cu10Ti10 HEA. (a) low-magnification image, (b) high-magnification image, (c) magnified image of the sample region marked in (b), (d) magnified image of square region in (a), (e) magnified image of square region in (d), (f) high-magnification SEM image of the grain interior in (d).

Table 1. Chemical compositions (in at.%) of the as-cast and the heat-treated Fe27Ni27Co26Cu10Ti10 HEA samples analyzed by SEM-EDS with the analyzed regions marked by different numbers in Figs. 3 and 4.

State	Num	Fe	Ni	Co	Cu	Ti					
	ber										
Nominal	_	27	27	26	10	10					
composition	1	30.80	26.16	26.42	8.87	7.75					
As-cast	2	14.85	29.88	25.17	9.30	20.80					
	3	21.74	28.43	24.97	10.66	14.20					
Heat-treated	4	30.21	25.02	26.93	9.04	8.80					
	5	13.22	33.87	25.52	7.49	19.90					

As depicted in Fig. 4(a), the heat-treated Fe₂₇Ni₂₇Co₂₆Cu₁₀Ti₁₀ HEA exhibits equiaxed grains similar to the as-cast sample, while the phase formed near the grain boundaries is different. Quite a lot of needle-like phase completely occupy the grain boundaries of the equiaxed grains, and have a tendency the into grain interior. high-magnification image (Fig. 4(a)), it is observed that this needle-like phase does not generate along one particular direction, but is interlaced with each other in different directions. The EDS result of point 4 (listed in Table 1) reveals that the chemical composition of the grain interior after heat treatment does not change significantly and remains close to the nominal composition. However, Ni and Ti are more obviously enriched in the needle-like phase of the heat-treated HEA. The chemical composition of the needle-like phase is as follows: Fe: 13.22, Ni: 33.87, Co: 25.52, Cu: 7.49, Ti: 19.90 at.%.

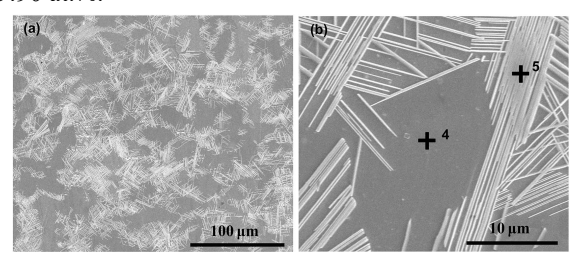


Fig. 4: SEM images of the heat-treated Fe27Ni27Co26Cu10Ti10 HEA. (a) low-magnification image, (b) high-magnification image.

To further investigate the crystal structure, morphology and elemental distribution of multiple phases in the as-cast Fe₂₇Ni₂₇Co₂₆Cu₁₀Ti₁₀ HEA, TEM analysis is conducted in Fig. 5. Figs. 5(a-b) are low-magnification bright-field (BF) TEM images of the region near the grain boundaries, illustrating that the needle-like phase grows along grain boundaries into intergranular and could cross two adjacent grains. Focusing on the region near the grain boundary, it is

surprisingly found that some smaller bright white particles precipitated together with the near-spherical precipitates observed in the SEM image, as shown in Fig. 5(c). The weak super-lattice diffraction spots in the SAED pattern in the inset along the [011] zone axis demonstrate the ordered fcc structure. There are also high-density nano-sized spherical precipitates within the intergranular, as depicted in Fig. 5(d). The corresponding SAED pattern confirms the ordered L1₂ structure of these nanoprecipitates in the grain interior and their coherent relationship with the fcc matrix.

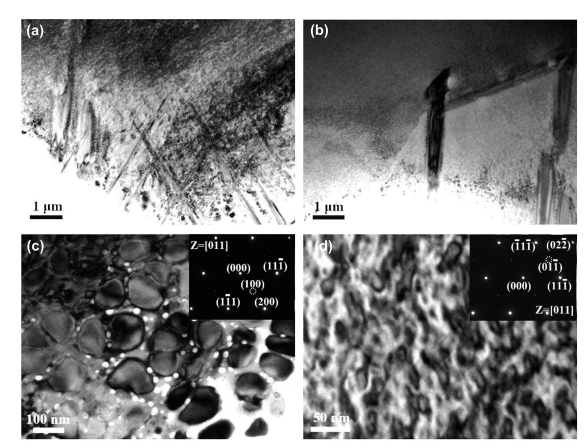


Fig. 5: TEM images of the as-cast Fe27Ni27Co26Cu10Ti10 HEA.

(a) and (b) low-magnification bright-field TEM images, (c)
bright-field TEM image of the region closed to grain boundary
with corresponding SAED pattern, (d) bright-field TEM image of
grain interior with corresponding SAED pattern.

The specific crystal structure of the needle-like is analyzed concretely in Fig. 6. The location of the needle-like phase is identified in the BF-TEM image (Fig. 6(a)). Then, the SAED pattern (Fig. 6(b)) corresponding to the selected area (indicated by the yellow circle in Fig. 6(a)) can be obtained. By comparing the standard electron diffraction pattern, the positions of the lattice represented by the diffraction spots are calibrated, and the crystal structure of the needle-like phase is determined to be the ordered $D0_{24}$ -type η phase. Additionally, the small bright white particles can be noted to generate in abundance in the interstices of large near-spherical precipitates in Fig. 6(a).

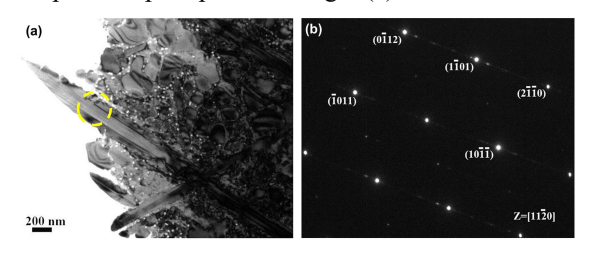


Fig. 6: TEM image of the needle-like η phase in the as-cast Fe27Ni27Co26Cu10Ti10 HEA. (a) bright-field TEM image, (b) SAED pattern corresponding to the needle-like η phase.

HR-TEM image of the as-cast Fe₂₇Ni₂₇Co₂₆Cu₁₀Ti₁₀ HEA in the grain interior is presented in Fig. 7. The interface between the precipitate and matrix, as manifested in Fig. 7(a), corroborates their fully coherent relationship. Figs. 7(b) and (d) are fast Fourier transform (FFT) patterns along the [011] zone axis corresponding to the matrix and precipitate, showing disordered fcc structure (A1) and ordered fcc structure (L1₂), respectively. HR-TEM image and FFT patterns provide further evidence of the "fcc+L1₂" structure in the grain interior.

The chemical compositions of the fcc matrix, precipitates and η phase in the as-cast sample can be obtained by EDS/TEM analysis, and the results are summarized in Table 2. The fcc matrix is significantly enriched in Fe and slightly enriched in Co, while being depleted in Ni-Cu-Ti. In contrast, Ni and Ti exhibit a strong tendency to enrich in the precipitates, whereas the contents of Fe and Cu in the precipitates are pretty low.

Interestingly, the η phase shares a similar chemical composition with the precipitates. It is also noteworthy that the content of Cu in these three phases is extremely low. Therefore, it is reasonable to assume that another bright white particle may have a very high degree of Cu enrichment.

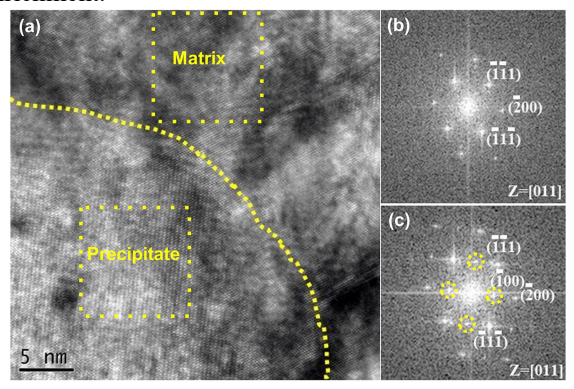


Fig. 7: HR-TEM of the as-cast Fe27Ni27Co26Cu10Ti10 HEA. (a) HR-TEM of the spherical precipitate and fcc matrix, (b) FFT of the matrix, showing fcc structure, (c) FFT of the precipitate, showing ordered fcc structure (L12).

Table 2. Chemical compositions (in at.%) of the as-cast and the heat-treated Fe27Ni27Co26Cu10Ti10 HEA samples analyzed by TEM-EDS and/or APT.

State	Measure method	Phase	Fe	Ni	Со	Cu	Ti
As-cast	EDS/TEM	fcc matrix	41.95±2.45	19.33±2.33	29.54±1.35	5.52±0.82	3.66±0.42
	EDS/TEM	Precipitate	7.46±1.09	39.74±0.18	27.36±0.99	4.56±0.80	20.88±0.85
	EDS/TEM	η	8.62±1.35	37.68±3.00	27.22±2.79	5.61±0.66	20.78±0.79
	APT	fcc matrix	49.94±1.95	17.46±1.48	29.09±1.78	1.10±0.40	2.41±0.59
	APT	Precipitate	6.05±0.87	43.70±1.83	25.49±1.61	1.01±0.38	23.75±1.57
	APT	White particles	0.89±0.79	9.14±3.66	0.75±0.67	87.55±4.28	1.67±0.89
Heat-treated	EDS/TEM	fcc matrix	30.59±1.31	23.18±0.42	26.00±0.46	10.49±1.71	9.74±0.88
	EDS/TEM	η	8.09±0.50	37.72±0.45	23.85±0.35	5.54±0.18	24.80±0.43

3D APT reconstruction near the grain boundaries in the as-cast Fe₂₇Ni₂₇Co₂₆Cu₁₀Ti₁₀ HEA quantitatively illustrates the elemental partitioning of the constituent atoms, as depicted in Fig. 8. Fig. 8(a) shows a 3D Ti-Cu map and two interfaces highlighted by 20 at.% Ti and 50 at.% Cu iso-concentration surface, respectively. The 20 at.% Ti iso-concentration map delineates the outline of the large near-spherical precipitates near the grain boundaries, while the 50 at.% Cu iso-concentration surface represents the outer contour of the small bright white particles. Two 1D concentration-depth profiles taken along the length direction of the cylinder "b" and "c" in (a) are displayed in Figs. 8(b) and (c), respectively. The chemical compositions of the fcc matrix, precipitates and bright white particles in the as-cast sample are summarized in Table 2. It can be concluded that Ni

(43.70 at.%) and Ti (23.75 at.%) are enriched in the large near-spherical precipitates, while the fcc matrix contains comparatively higher Fe (49.94 at.%), as shown in Fig. 8(b). In contrast, the bright white particle exhibits an extremely high content of Cu (87.55 at.%) and a slight Ni (9.14 at.%), with almost no other constituent elements (Fe:0.89 at.%, Co:0.75 at.%, Ti:1.67 at.%). This elemental distribution verifies that the conjecture in the above section is current and sensible.

The chemical compositions of the fcc matrix and precipitates obtained by the APT method are consistent with the EDS/TEM results. Combined with the SAED pattern in Fig. 5(c), it can be determined that the large near-spherical precipitates near the grain boundaries are ordered L1₂ precipitates. According to the previous research, the stoichiometry of the L1₂ precipitates could

be regarded as (Ni,Co)₃Ti [12, 13]. The bright white particle contains almost 90 at.%, which can be approximately considered a pure Cu particle. The crystal structure of Cu atomic is disordered fcc, so the Cu-rich bright white particles can be determined to be fcc structure. The diffraction spots corresponding to the Cu-rich particles are overlapped with the fcc matrix,

resulting in the "fcc+L1₂" structure illustrated by the SAED pattern in Fig. 5(c). In summary, the as-cast Fe₂₇Ni₂₇Co₂₆Cu₁₀Ti₁₀ HEA consists of the fcc matrix with L1₂ nanoprecipitates in the intergranular, and needle-like η phase, large near-spherical L1₂ precipitates and Cu-rich particles near the grain boundaries.

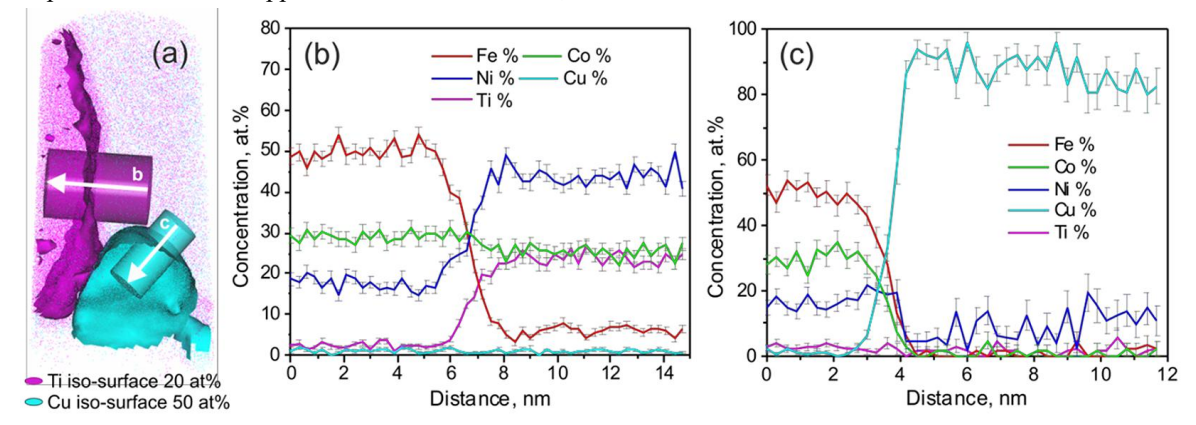


Fig. 8: APT analysis revealing elemental distributions across interfaces in the as-cast Fe27Ni27Co26Cu10Ti10 HEA. (a) 3D Ti-Cu map and two interfaces highlighted by 20 at. % Ti and 50 at. % Cu iso-concentration surfaces, respectively; (b) and (c) are 1D compositional profiles taken along the length direction of the cylinder "b" and "c" in (a), respectively.

Fig. 9 shows representative TEM images of the heat-treated Fe₂₇Ni₂₇Co₂₆Cu₁₀Ti₁₀ HEA near the grain boundaries. Some needle-like phases along various directions are embedded within the matrix, as manifested in Fig. 9(a). The SAED pattern presented in Fig. 9(b) along the [011] zone axis corresponds to a disordered fcc structure without weak superlattice spots, suggesting no precipitates within the fcc matrix. A typical η -D0₂₄ structure is illustrated by the SAED pattern (Fig. 9(c)) along the [11 $\bar{2}$ 0] zone axis, indicating the crystal structure of the needle-like phase.

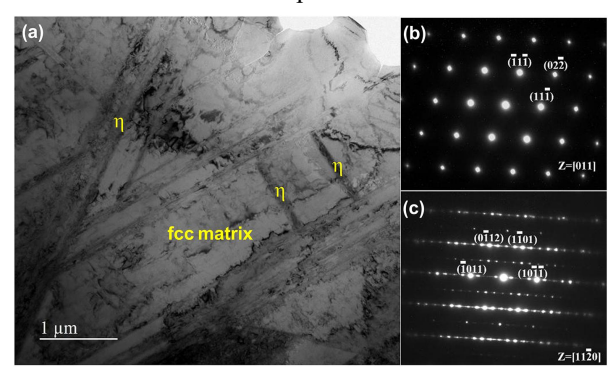


Fig. 9: TEM images of the heat-treated Fe27Ni27Co26Cu10Ti10 HEA. (a) bright-field TEM image, (b) SAED pattern of the fcc matrix, (c) SAED pattern of the needle-like η phase.

The elemental distribution of the heat-treated Fe₂₇Ni₂₇Co₂₆Cu₁₀Ti₁₀ HEA is characterized by high-angle annular dark-field scanning transmission electron microscopy (HAADF-STEM) image and its corresponding EDS elemental mapping (Fig. 10). It can

be observed that Ni and Ti have a strong tendency to enrich in η phase, while all constituent elements exhibit homogenous distribution in the fcc matrix. Hence, the absence of elemental segregation in the fcc matrix confirms that no precipitate is formed. Furthermore, the EDS/TEM results (Table 2) reveal a η -type phase with a detailed composition of \sim 8.09 at.% (Fe), \sim 37.72 at.% (Ni), \sim 23.85 at.% (Co), \sim 5.54 at.% (Cu), \sim 24.80 at.% (Ti), which is consistent with the chemical composition of the η phase in the as-cast HEA. Based on previously reported studies, the needle-like η phase presented in both the as-cast and heat-treated HEAs can be classified as a Ni₃Ti-type intermetallic with the D0₂₄ structure [26]. In conclusion, the heat-treated Fe₂₇Ni₂₇Co₂₆Cu₁₀Ti₁₀ HEA is composed of a fcc matrix with an amount of η phase.

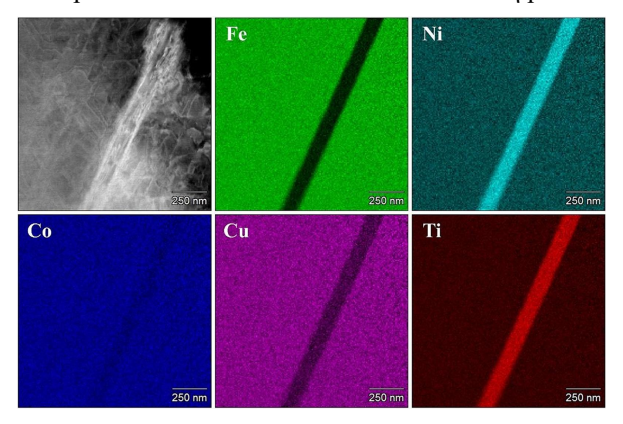


Fig. 10: HADDF-STEM EDS mapping of the heat-treated Fe27Ni27Co26Cu10Ti10 HEA, showing that component elements are uniformly distributed in the fcc matrix, whereas the needle-like η phase is Ni-Ti rich.

The EDS/TEM and APT results indicate that the chemical compositions of the L1₂ precipitates and needle-like η phase are highly consistent, both the L1₂ precipitates and η phase display a noticeable tendency to enrich Ni, Co and Ti. This elemental enrichment tendency can be explained by the difference in mixing enthalpy between the constituent elements. The more negative mixing enthalpy of Ni-Ti (-35 kJ/mol) and Co-Ti (-28 kJ/mol) atom pairs facilitate the formation of the (Ni,Co)₃Ti-type phase with ordered L1₂ and D0₂₄ structure [²⁷].

The existence of the Cu-rich particles precipitated near the grain boundaries in the as-cast HEA could be due to the positive mixing enthalpy between Cu and other components, for example, Cu-Fe: 13 kJ/mol, Cu-Co: 6 kJ/mol and Cu-Ni: 4 kJ/mol. Although the Cu-Ti atom pair has a negative mixing enthalpy, its value (-9 kJ/mol) is still apparently higher than the Ni-Ti and Co-Ti atom pairs, thus Ti preferentially assists the nucleation of the L₁₂ precipitates [26, 28]. The large near-spherical L₁₂ precipitates formed near the grain boundaries consume almost all of the Ti, resulting in small bright white particles that can be seen as almost pure Cu formed between the L1₂ precipitates. These Cu-rich particles then can act as heterogeneous nucleation sites to accelerate the formation of the L1₂ precipitates, culminating in a dense co-precipitation structure [29].

The distorted atomic arrangement at the interface gives grain boundaries higher energy than transgranular, and this high-energy state encourages the grain boundaries to lower the nucleation energy barrier of the precipitates by providing additional driving force [30]. Additionally, the solute atoms at the grain boundaries have a higher diffusion ability due to interface reaction and thus are more likely to aggregate together to form clusters or phases [31, 32]. Grain boundaries are the interfaces between grains with different orientations in polycrystalline materials, which can also be considered a crystal defeat to serve as non-homogeneous nucleation sites [33]. Therefore, multiple phases, including L12 precipitates, Cu-rich particles and needle-like n phase, are generated near the grain boundaries of the as-cast $Fe_{27}Ni_{27}Co_{26}Cu_{10}Ti_{10}$ HEA.

Based on the above microstructure analysis, it can be concluded that a significant phase transformation occurs in Fe₂₇Ni₂₇Co₂₆Cu₁₀Ti₁₀ HEA after heat treatment at 1000°C for 2 h. Specifically, the phase evolution can be summarized as fcc+Ll₂+Cu-rich+ η phases to fcc+ η phases. The Ll₂ precipitates and Cu-rich particles may dissolve into the fcc matrix or transform to η phase

during the high-temperature heat treatment. The specific reasons for the disappearance of the L1₂ precipitates and Cu-rich particles in heat-treated HEA are discussed below.

The L1₂ and η-D0₂₄ structures are related by different stacking sequences of identical close-packed ordered planes [34, 35]. The η-D0₂₄ phase exhibits an atomic arrangement of ABACABAC along the [0001]_n direction, whereas the orders of the close-packed plane of the L1₂ phase follow the ABCABC law along the [111]_{L12} direction. The atomic plane with an interface orientation relation of $(0001)_n/(111)_{L12}$ provides the necessary condition for the transformation of the L12 and η -D024 structures [24]. Another essential condition for the crystal structure transition from L1₂ to η-D0₂₄ is the extrinsic stacking faults (ESFs) caused by the climb of Frank dislocation partials [34]. Even if the above necessary conditions are fulfilled, sufficient driving force is still required to realize the L1₂ to η-D0₂₄ phase transition. As well known, the lattice misfit between the η phase and fcc matrix is significantly larger than fcc and L1₂ with complete coherency, resulting in larger strain energy of the n phase. Additionally, the thermodynamic driving force offered by the high-temperature heat treatment facilitates the phase transformation.

The η-D0₂₄ phase forms at the expense of the L1₂ phase, and its chemical composition, (Ni,Co)₃Ti, is the same as that of the L1₂ phase. This leads to a deficiency of the constituent elements necessary for the nucleation of the L1₂ phase and lowers the degree of supersaturation in the fcc matrix, making it more difficult for the L12 phase to form. Furthermore, the abundant needle-like η phase precipitated at the grain boundaries plays a key role in adsorbing and storing the impurities and defects, which decreases the interfacial energy and defect density in the grain boundary region [25, 36]. As a consequence, the reduction in heterogeneous nucleation sites and the driving force both improve the difficulty of nucleation. Therefore, when the η-D0₂₄ phase fully occupies the grain boundaries, the formation of other phases (L12 precipitates and Cu-rich particles) is strongly suppressed. Moreover, the η-D0₂₄ phase can effectively pin the grain boundaries, thus inhibiting grain boundary migration from the kinetics perspective. This decrease in the grain boundary migration rate also suppresses the nucleation of the precipitates near the grain boundaries [37].

3.2 Mechanical behaviours

Fig. 11 displays the representative tensile engineering stress-strain curves of the as-cast and heat-treated $Fe_{27}Ni_{27}Co_{26}Cu_{10}Ti_{10}$ HEA at room temperature. The

specific values of the mechanical properties, including the yield strength ($\sigma_{0.2}$), ultimate tensile strength (σ_{UTS}), and total elongation, are summarized in Table 3. The as-cast HEA exhibits a notable strength-ductility trade-off, with a superior yield strength of ~1020 MPa, yet a poor total elongation of ~0.9%. Compared to the as-cast HEA, the heat-treated HEA demonstrates significantly improved ductility, with total elongation increasing to ~7.5%. Meanwhile, the sacrifice in the strength of the heat-treated HEA remains within acceptable limits, the yield strength and ultimate tensile strength are ~662 MPa and ~925 MPa, respectively.

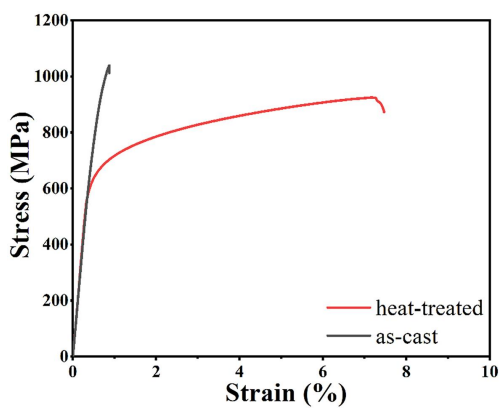


Fig. 11: Representative tensile engineering stress–strain curves of the as-cast and heat-treated Fe27Ni27Co26Cu10Ti10 HEA samples at room temperature.

To further investigate the mechanical behaviours during tensile deformation, the fracture morphology of both the as-cast and heat-treated samples after tensile tests is illustrated in Fig. 12. As displayed in Fig. 12(a), a large cleavage facet can be observed in the as-cast sample. Fig. 12(b) presents the fracture morphology in the region near grain boundaries, where thin, elongated cleavage facets in multiple directions coincide with the shape of the needle-like η phase (indicated by the yellow dash line). This observation demonstrates that the cracks propagate along the n phase during tensile deformation. The dense dimples shown in Fig. 12(c) are associated with the dispersive distribution of the L1₂ precipitate within the grain interior of the as-cast sample. Published studies have indicated that when the size of dimples is comparable to the spacing of the inclusions, the η phase may promote the formation of microvoids. Consequently, cracks tend to propagate through the weak interfaces with relatively low cohesion forces [18]. As a result, the as-cast samples experience premature brittle fracture during the tensile process.

As manifested in Figs. 12(d-e), different from the as-cast sample, the fracture morphology of the heat-treated sample exhibits significantly denser and more multidirectional, thin and long cleavage facets. These cleavage facets with the compatible shapes of the needle-like η phase intersect with each other and completely cover the entire fracture. In the enlarged SEM image (Fig. 12(f)), a small amount of dimples can be observed in the gap between the thin and long cleavage facets. The high-density needle-like η phase in different directions can intercept each other, effectively preventing the expansion of plastic deformation-induced cracks.

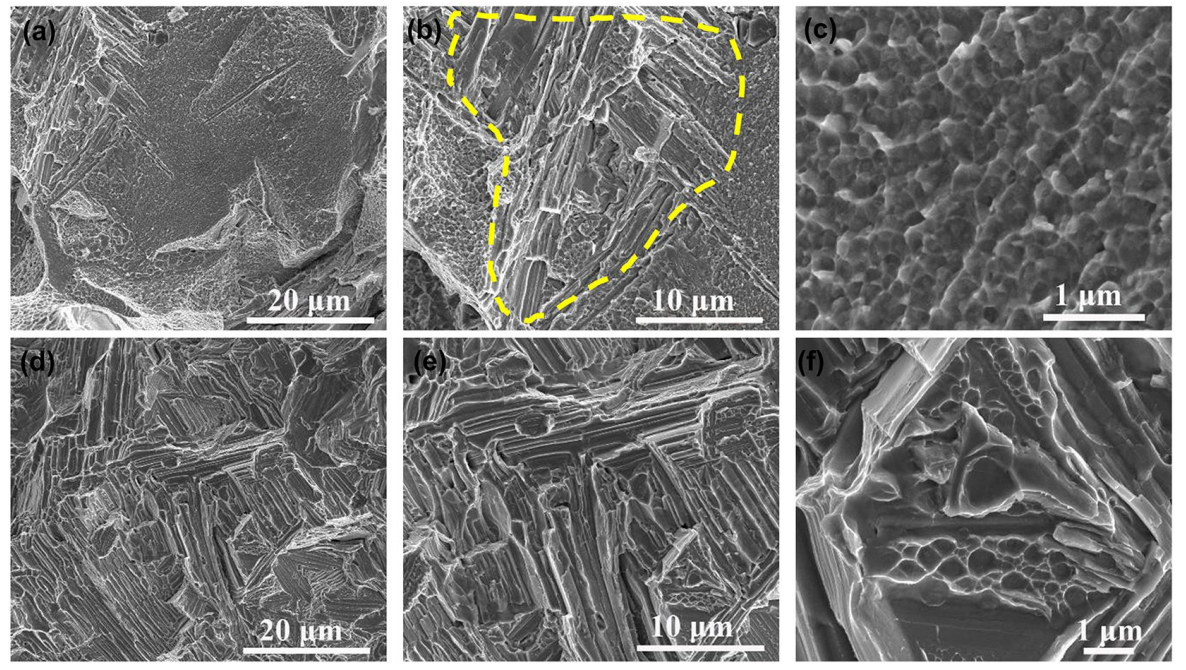


Fig. 12: Fracture morphologies of HEA samples after tension tests. (a), (b) and (c) as-cast; (d), (e) and (f) heat-treated.

The η phase exhibits an ordered Ni₃Ti-type hcp structure, and has a specific orientation relationship with the disordered fcc phase, that is, $\{1\,\bar{1}\,1\}_{fcc}//\{0001\}_{\eta}$ and $[011]_{fcc}//[11\,\bar{2}\,0]_{\eta}$ [38]. The interfacial relationship between the η phase and fcc phase can be classified into two types: the non-coherent interface corresponding to the tip of the η phase, and the coherent interface associated with the macroscopically elongated side [27]. The tip of the η phase, which features a non-coherent interface, acts as the growth front of the phase due to its higher interfacial energy. As a result, the phase grows along the macroscopically elongated direction, and this interfacial characteristic contributes to the needle-like morphology of the η phase.

The needle-like η phase greatly influences the mechanical properties of the heat-treated HEA. At the macro level, the needle-like η phase can deflect cracks during propagation, leading to the formation of more zigzag and jagged cracks. This deflection process consumes more energy, making it harder for cracks to continue propagating [39, 40]. From the micro perspective, the needle-like n phase contributes to pinning the interface and impede the movement of dislocations. Meanwhile, the η/fcc interface with a certain degree of lattice mismatch enables the η phase to serve as the dislocation source to generate new dislocations as strain increases [41]. The macroscopic effect on cracks and microscopic effect on dislocations of the needle-like η phase synergistically affect the mechanical behaviours of the heat-treated HEA.

The heterogeneous co-precipitation structure near the grain boundaries in the as-cast HEA is detrimental to the ductility, which is the primary cause of premature brittle fracture. After high-temperature heat treatment, the structure of the near grain boundary region transforms into a dense network of needle-like η phase that interspersed with each other. As discussed above, the needle-like η phase can strongly hinder the propagation of the cracks, contributing to the improvement of the ductility. Furthermore, unlike the fcc+L12 structure in the grain interior of the as-cast HEA, the heat-treated HEA exhibits a single-phase fcc-structured transgranular without any precipitates. The softer single-phase fcc structure possesses greater dislocation storage capacity and load bearing capacity, which is also conducive to enhancing the ductility of the alloy [42]. In summary, the phase transformation from fcc+L1₂+Cu-rich+η phases in the as-cast HEA to fcc+η phases in the heat-treated HEA significantly improves the comprehensive mechanical properties of the materials, highlighting the strengthening effect of the sole η phase in fcc-structured HEAs.

4 Conclusions

In this work, the as-cast and heat-treated Fe₂₇Ni₂₇Co₂₆Cu₁₀Ti₁₀ HEA samples were successfully designed and fabricated. The microstructure evolution, phase transformation and mechanical behaviours were systematically investigated. Based on the studies carried out, the main findings are as follows:

- The microstructure evolution could be summarized as fcc+L1₂+Cu-rich+ η phases in the as-cast HEA to fcc+ η phases in the heat-treated HEA. The formation of the L1₂ and Cu-rich phases was significantly suppressed during high-temperature heat treatment. The phase transition between the L1₂ and η -D0₂₄ phases is also analyzed in detail.
- The mechanical properties of the heat-treated HEA were significantly improved compared to the as-cast HEA, and the total elongation increased from $\sim 0.9\%$ to $\sim 7.5\%$. At the same time, the yield strength and ultimate tensile strength remained at ~ 662 MPa and ~ 925 MPa, respectively. The needle-like η phase affected the mechanical behaviours by impeding crack expansion and dislocation movement. Additionally, the soft single-phase fcc-structured transgranular also contributed to the increase in ductility.
- This work sheds light on understanding the strengthening mechanisms of the sole η -D0₂₄ phase in the fcc-structured HEAs, providing a new approach for enhancing mechanical properties and broadening the research potential of precipitate-strengthened alloys.

Acknowledgments

Liran Huang, Weiping Chen and Zhiqiang Fu wish to the National acknowledge Key Research Development Program of China (Grant No. 2024YFB4608600), the International Science Technology Cooperation Project of Guangdong Province (Grant No. 2023A0505050154), the Basic and Applied Basic Research Foundation of Guangdong Province (Grant No. 2023A1515012363), the National Natural Science Foundation of China (Grant No. 52103360), the Pearl River Talent Program (Grant No. 2021QN02C766) and the technical support of Sinoma Institute of Materials Research (Guang Zhou) Co., Ltd.

Conflicts of interest:

The authors declare that they have no known competing financial interests or personal relationships that could have appeared to influence the work reported in this paper.

References

- [1] Mu Y, He L, Deng S, et al. A high-entropy alloy with dislocation-precipitate skeleton for ultra-strength and ductility. Acta Mater. 2022, 232: 117975, https://doi.org/10.1016/j.actamat.2022.117975.
- [2] Pan Q, Zhang L, Feng R, et al. Gradient cell–structured high-entropy alloy with exceptional strength and ductility. Science. 2021, 374(6570): 984-989, https://doi.org/10.1126/science.abj8114.
- [3] Liu S, Duan J, Zhang M, et al. Correlation of microstructure, mechanical properties and corrosion behavior in a Ni₃₄Co₂₈Cr₂₈Al₁₀ multi-principal element alloy with outstanding corrosion resistance. Corros. Sci. 2024, 228(1): 111835, https://doi.org/10.1016/j.corsci.2024.111835.
- [4] Moravcik I, Hornik V, Minárik P, et al. Interstitial doping enhances the strength-ductility synergy in a CoCrNi medium entropy alloy. Mater. Sci. Eng. A. 2020, 781(4): 1-14, https://doi.org/10.1016/j.msea.2020.139242.
- [5] Ding L, Hilhorst A, Idrissi H, et al. Potential TRIP/TWIP coupled effects in equiatomic CrCoNi medium-entropy alloy. Acta Mater. 2022, 234: 118049, https://doi.org/10.1016/j.actamat.2022.118049.
- [6] Gludovatz B, Hohenwarter A, Thurston K V S, et al. Exceptional damage-tolerance of a medium-entropy alloy CrCoNi at cryogenic temperatures. Nat. Commun. 2016, 7: 1-8, http://dx.doi.org/10.1038/ncomms10602.
- [7] Otto F, Dlouhý A, Somsen C, et al. The influences of temperature and microstructure on the tensile properties of a CoCrFeMnNi high-entropy alloy. Acta Mater. 2013, 61(15): 5743-5755, https://doi.org/10.1016/j.actamat.2013.06.018.
- [8] Liu L, Zhang Y, Han J, et al. Nanoprecipitate-Strengthened High-Entropy Alloys. Adv. Sci. 2021: 1-20, https://doi.org/10.1002/advs.202100870.
- [9] Gangireddy S, Gwalani B, Mishra R S. Grain size dependence of strain rate sensitivity in a single phase FCC high entropy alloy Al_{0.3}CoCrFeNi. Mater. Sci. Eng. A. 2018, 736(8): 344-348, https://doi.org/10.1016/j.msea.2018.09.009.
- [10] Coury F G, Wilson P, Clarke K D, et al. High-throughput solid solution strengthening characterization in high entropy alloys. Acta Mater. 2019, 167: 1-11, https://doi.org/10.1016/j.actamat.2019.01.029.
- [11] Chu C, Chen W, Huang L, et al. Exceptional strength-ductility synergy at room and liquid nitrogen temperatures of Al_{7.5}Co_{20.5}Fe₂₄Ni₂₄Cr₂₄ high-entropy alloy with hierarchical precipitate heterogeneous structure. Int. J. Plast. 2024, 175(12): 103939, https://doi.org/10.1016/j.ijplas.2024.103939.
- [12] He J Y, Wang H, Huang H L, et al. A precipitation-hardened high-entropy alloy with outstanding

- tensile properties. Acta Mater. 2016, 102: 187-196, https://doi.org/10.1016/j.actamat.2015.08.076.
- [13] Zhao Y L, Yang T, Tong Y, et al. Heterogeneous precipitation behavior and stacking-fault-mediated deformation in a CoCrNi-based medium-entropy alloy. Acta Mater. 2017, 138: 72-82, https://doi.org/10.1016/j.actamat.2017.07.029.
- [14] Yang T, Zhao Y L, Fan L, et al. Control of nanoscale precipitation and elimination of intermediate-temperature embrittlement in multicomponent high-entropy alloys. Acta Mater. 2020: 47-59, https://doi.org/10.1016/j.actamat.2020.02.059.
- [15] Yen S yu, Liu Y chen, Chu S hsiang, et al. B2-strengthened Al-Co-Cr-Fe-Ni high entropy alloy with high ductility. Mater. Lett. 2022, 325(6): 132828, https://doi.org/10.1016/j.matlet.2022.132828.
- [16] Jo Y H, Choi W M, Sohn S S, et al. Role of brittle sigma phase in cryogenic-temperature-strength improvement of non-equi-atomic Fe-rich VCrMnFeCoNi high entropy alloys. Mater. Sci. Eng. A. 2018, 724(4): 403-410, https://doi.org/10.1016/j.msea.2018.03.115.
- [17] Lin K, Chen S C, Lin H C, et al. Enhancement in mechanical properties through an FCC-to-HCP phase transformation in an Fe-17.5Mn-10Co-12.5Cr-5Ni-5Si (in at%) medium-entropy alloy. J. Alloys Compd. 2022, 898: 162765, https://doi.org/10.1016/j.jallcom.2021.162765.
- [18] Shen P K, Liu H C, Huang C Y, et al. Microstructure and mechanical properties of medium-entropy alloys with a high-density η-D0₂₄ phase. Mater. Charact. 2022, 185(101): 111713. https://doi.org/10.1016/j.matchar.2021.111713.
- [19] Fan L, Yang T, Zhao Y, et al. Ultrahigh strength and ductility in newly developed materials with coherent nanolamellar architectures. Nat. Commun. 2020, 11(1): 1-8, http://dx.doi.org/10.1038/s41467-020-20109-z.
- [20] Chou T H, Li W P, Chang H W, et al. Suppressing temperature-dependent embrittlement in high-strength medium-entropy alloy via hetero-grain/precipitation engineering. Scr. Mater. 2023, 229(2), https://doi.org/10.1016/j.scriptamat.2023.115377.
- [21] Zhao Y L, Yang T, Zhu J H, et al. Development of high-strength Co-free high-entropy alloys hardened by nanosized precipitates. Scr. Mater. 2018, 148: 51-55, https://doi.org/10.1016/j.scriptamat.2018.01.028.
- [22] Hou Y D, Li X N, Li Z M, et al. Achieving optimal comprehensive properties in heat resistant Cu-based alloys by regulating complex elemental interaction. Mater. Charact. 2024, 216(5), https://doi.org/10.1016/j.matchar.2024.114308.
- [23] Yuan J L, Wu Y C, Liaw P K, et al. Remarkable cryogenic strengthening and toughening in nano-coherent

- CoCrFeNiTi_{0.2} high-entropy alloys via energetically-tuning polymorphous precipitates. Mater. Sci. Eng. A. 2022, 842(1), https://doi.org/10.1016/j.msea.2022.143111.
- [24] Chu C, Chen W, Fu Z, et al. Realizing good combinations of strength-ductility and corrosion resistance in a Co-free Fe₄Ni₄Mn₂CrTi high-entropy alloy via tailoring Ni/Ti-rich precipitates and heterogeneous structure. Mater. Sci. Eng. A. 2023, 878(4): 145223, https://doi.org/10.1016/j.msea.2023.145223.
- [25] Ou M, Ma Y, Ge H, et al. Microstructure evolution and mechanical properties of a new cast Ni-base superalloy with various Ti contents. J. Alloys Comp. 2018, 735: 193-201, https://doi.org/10.1016/j.jallcom.2017.11.074.
- [26] Chu C, Hao L, Chen W, et al. Phase transformations and mechanical behavior in a non-equiatomic Ti10Fe30Co30Ni30 medium-entropy alloy. Mater. Sci. Eng. A. 2022, 832(12): 142429, https://doi.org/10.1016 /j.msea.2021.142429.
- [27] Zhang B, Mu W, Cai Y. The effect of cooling rate on the precipitation behavior and fracture toughness of the η phase in LDED CoCrFeNiTi high-entropy alloy. Mater. Sci. Eng. A. 2024, 914(8): 147172, https://doi.org/10.1016/j.msea.2024.147172.
- [28] Sharma A, Lee H, Ahn B. Tailoring compressive strength and absorption energy of lightweight multi-phase alcusifex (X = cr, mn, zn, sn) high-entropy alloys processed via powder metallurgy. Materials. 2021, 14(17), https://doi.org/10.3390/ma14174945.
- [29] Gwalani B, Gorsse S, Soni V, et al. Role of copper on L1₂ precipitation strengthened fcc based high entropy alloy. Materialia. 2019, 6(1): 100282, https://doi.org/10.1016/j.mtla.2019.100282.
- [30] Kokkula P C, Samanta S, Mandal S, et al. Kinetics of pearlite transformation: The effect of grain boundary engineering. Acta Mater. 2025, 284(7): 120641, https://doi.org/10.1016/j.actamat.2024.120641.
- [31] Jägle E A, Mittemeijer E J. The kinetics of grain-boundary nucleated phase transformations: Simulations and modelling. Acta Mater. 2011, 59(14): 5775-5786, http://dx.doi.org/10.1016/j.actamat.2011.05.054.
- [32] Wang Z, Xiao H, Chen W, et al. Effect of grain boundary and reinforced particles on grain boundary precipitates in TiB2/Al-Zn-Mg-Cu composite. Mater. Charact. 2023, 197(12): 112703, https://doi.org/10.1016/j.matchar.2023.112703.

- [33] Yao Y, Euesden R, Curd M E, et al. Effect of cooling rate on the composition and chemical heterogeneity of quench-induced grain boundary η-phase precipitates in 7xxx aluminium alloys. Acta Mater. 2024, https://doi.org/10.1016/j.actamat.2023.119443.
- [34] Kear B H, Giamei A F, Silcock J M, et al. Slip and climb processes in γ' precipitation hardened nickel-base alloys. Scr. Metall. 1968, 2(5): 287-293, https://doi.org/10.1016/0036-9748(68)90123-3.
- [35] Hagihara K, Nakano T, Umakoshi Y. Plastic deformation behaviour in Ni3Ti single crystals with D0₂₄ structure. Acta Mater. 2003, 51(9): 2623-2637, https://doi.org/10.1016/S1359-6454(03)00060-0.
- [36] Ma S, Wang M, Ju Y, et al. Atomic-scale observation of the interfaces between η and γ matrix in ATI718Plus. Mater. Charact. 2024, 215(7): 114196, https://doi.org/10.1016/ j.matchar.2024.114196.
- [37] Ouyang H, Li Y, Guo C, et al. Differential effects of Fe, Ti and Fe + Ti addition on the discontinuous precipitation and properties of Cu-Ni-Sn alloys. Mater. Charact. 2024, 212(1), https://doi.org/10.1016/j.matchar.2024.114007.
- [38] Suk J I, Hong S H, Nam S W. Crystallographic orientation relationships among η-Ni₃Ti precipitate, reverted austenite, and martensitic matrix in Fe-10Cr-10Ni-2W maraging alloy. Metall. Trans. A. 1993, 24(12): 2643-2652, https://doi.org/10.1007/BF02659488.
- [39] Williams W M, Shabani M, Jablonski P D, et al. Fatigue crack growth behavior of the quaternary 3d transition metal high entropy alloy CoCrFeNi. Inter. J. Fatigue. 2021, 148(12): 106232, https://doi.org/10.1016/j.ijfatigue.2021.106232.
- [40] Pineau A. Crossing grain boundaries in metals by slip bands, cleavage and fatigue cracks. Philosophical Transactions of the Royal Society A: Mathematical, Phys. Eng. Sci. 2015, 373(2038), https://doi.org/10.1098/ rsta.2014.0131.
- [41] Zhai T, Jiang X P, Li J X, et al. The grain boundary geometry for optimum resistance to growth of short fatigue cracks in high strength Al-alloys. Inter. J. Fatigue. 2005, 27(10-12): 1202-1209, https://doi.org/10.1016/j.ijfatigue.2005.06.021.
- [42] Jiang K, Zhang Q, Li J, et al. Abnormal hardening and amorphization in an FCC high entropy alloy under extreme uniaxial tension. Inter. J. Plast. 2022, 159(8): 103463, https://doi.org/10.1016/j.ijplas.2022.103463.